



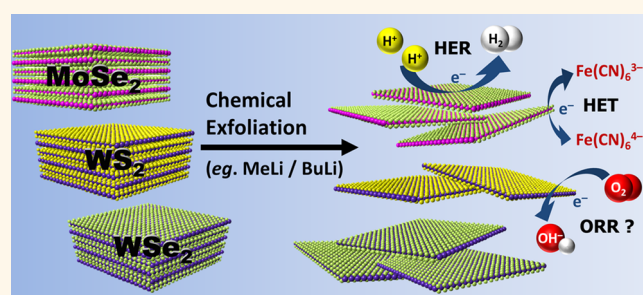
# Electrochemistry of Transition Metal Dichalcogenides: Strong Dependence on the Metal-to-Chalcogen Composition and Exfoliation Method

Alex Yong Sheng Eng,<sup>†</sup> Adriano Ambrosi,<sup>†</sup> Zdeněk Sofer,<sup>‡</sup> Petr Šimek,<sup>‡</sup> and Martin Pumera<sup>\*,†</sup>

<sup>†</sup>Division of Chemistry & Biological Chemistry, School of Physical and Mathematical Sciences, Nanyang Technological University, Singapore 637371, Singapore and

<sup>‡</sup>Department of Inorganic Chemistry, Institute of Chemical Technology, 166 28 Prague 6, Czech Republic

**ABSTRACT** Beyond MoS<sub>2</sub> as the first transition metal dichalcogenide (TMD) to have gained recognition as an efficient catalyst for the hydrogen evolution reaction (HER), interest in other TMD nanomaterials is steadily beginning to proliferate. This is particularly true in the field of electrochemistry, with a myriad of emerging applications ranging from catalysis to supercapacitors and solar cells. Despite this rise, current understanding of their electrochemical characteristics is especially lacking. We therefore examine the inherent electroactivities of various chemically exfoliated TMDs (MoSe<sub>2</sub>, WS<sub>2</sub>, WSe<sub>2</sub>) and their implications for sensing and catalysis of the hydrogen evolution and oxygen reduction reactions (ORR). The TMDs studied are found to possess distinctive inherent electroactivities and together with their catalytic effects for the HER are revealed to strongly depend on the chemical exfoliation route and metal-to-chalcogen composition particularly in MoSe<sub>2</sub>. Despite its inherent activity exhibiting large variations depending on the exfoliation procedure, it is also the most efficient HER catalyst with a low overpotential of  $-0.36$  V vs RHE (at  $10$  mA cm<sup>-2</sup> current density) and fairly low Tafel slope of  $\sim 65$  mV/dec after BuLi exfoliation. In addition, it demonstrates a fast heterogeneous electron transfer rate with a  $k^0_{\text{obs}}$  of  $9.17 \times 10^{-4}$  cm s<sup>-1</sup> toward ferrocyanide, better than that seen for conventional glassy carbon electrodes. Knowledge of TMD electrochemistry is essential for the rational development of future applications; inherent TMD activity may potentially limit certain purposes, but intended objectives can nonetheless be achieved by careful selection of TMD compositions and exfoliation methods.



**KEYWORDS:** transition metal chalcogenides · dichalcogenides · two-dimensional materials · chemical exfoliation · electrochemistry

Many layered transition metal dichalcogenides (TMDs) naturally occur in Earth's crust as mineral ores. Indeed, the most widely studied TMD material (molybdenum disulfide) is itself the primary source of molybdenum metal and exists as the mineral molybdenite.<sup>1</sup> In spite of the large number of other TMDs available in nature, a sizable percentage of contemporary literature is devoted almost exclusively to MoS<sub>2</sub>, with others progressively emerging. Most interestingly though, the properties of these TMD materials in their bulk states vastly differ from their exfoliated counterparts in the nanoscale regime, and efforts at obtaining two-dimensional (2D) layered TMDs are ongoing since initial reports in the 1970s.<sup>2–4</sup> More recently, the current scientific fervor in

2D layered nanomaterials first brought about by graphene has led to the fortuitous resurgence of interest in TMDs,<sup>5–7</sup> which extends to further include analogues such as boron nitride, silicene, and germanene.<sup>8,9</sup>

To date, numerous reports have demonstrated the effective use of layered TMDs for advanced energy storage, conversion, electrochemical catalysis, and sensing,<sup>10</sup> including Li-ion batteries,<sup>11</sup> supercapacitors,<sup>12</sup> and solar cells.<sup>13</sup> Of particular note is their efficiency toward the hydrogen evolution reaction (HER).<sup>14–17</sup> Conceivably, such applications require the synthesis of substantial amounts of material and consequently place a limit on their mass production potential. Just in this regard, liquid-phase exfoliation approaches<sup>4,16,18</sup> and colloidal

\* Address correspondence to pumera.research@gmail.com.

Received for review July 13, 2014 and accepted November 21, 2014.

Published online December 02, 2014  
10.1021/nn503832j

© 2014 American Chemical Society

solution syntheses<sup>19,20</sup> may present an advantage at the current stage of development, although mechanical exfoliation<sup>21,22</sup> and chemical vapor deposition<sup>23,24</sup> techniques also offer benefits that include higher purities, more pristine conditions, and control of size and layer thickness. Some of these factors represent real problems faced by the liquid-phase exfoliation approach in spite of its popularity, and a greater understanding of exfoliation processes and TMD properties is required to address such challenges.

Despite extensive research with varied directions in the field ranging from synthesis methods to device development, a general literature search reveals a comparative lack of basic knowledge on the inherent electrochemical properties of TMDs, especially after the exfoliation of their layers. In light of current interest to exploit TMDs for a myriad of electrochemical applications, we therefore believe that a fundamental study of TMD exfoliation and its resulting consequences on their material and inherent electrochemical properties is opportune and prudent. Toward this aim, we first perform exfoliation using lithium intercalants of varying strengths, with subsequent correlation of changes in intrinsic properties with the exfoliation extent. A systematic characterization of the materials is achieved using scanning electron microscopy (SEM), energy dispersive X-ray spectroscopy (EDS), Raman spectroscopy, X-ray photoelectron spectroscopy (XPS), and

surface area measurements based on methylene blue adsorption. We also perform voltammetric and XPS characterizations of the inherent electrochemistry of the materials with solid-state electrode modification. Finally, the implications of TMD exfoliation on electrocatalytic applications are explored in detail for the hydrogen evolution and oxygen reduction reactions, with additional calculations of the intrinsic heterogeneous electron transfer rates at these surfaces.

## RESULTS AND DISCUSSION

In this fundamental study, we investigate the effects of chemical exfoliation on the consequent material and electrochemical properties of transition metal dichalcogenides, namely, MoSe<sub>2</sub>, WS<sub>2</sub>, and WSe<sub>2</sub>. Additionally, their viability as electrocatalysts for the hydrogen evolution reaction and oxygen reduction reaction (ORR) is examined. While butyllithium (BuLi) is traditionally used in chemical exfoliation, little is understood regarding the effects of the accompanying alkyl moiety and its impact on the exfoliation. Thus, methylolithium (MeLi) is alternatively employed, and we evaluate its effectiveness.

**Chemical Exfoliation of Transition Metal Dichalcogenides.** In line with our first objective of studying the exfoliation efficiency using different organolithium intercalants, we examine the surface morphologies of the products by SEM. Figure 1 shows the electron micrographs of the

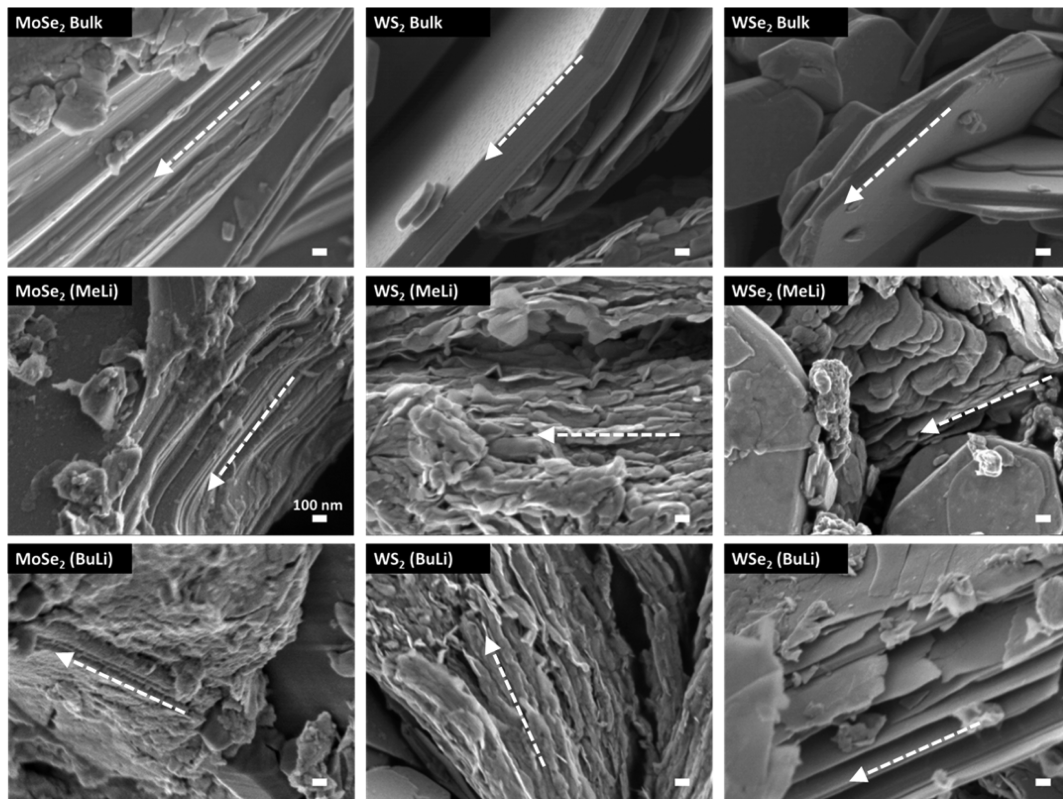


**Figure 1.** Scanning electron micrographs of MoSe<sub>2</sub>, WS<sub>2</sub>, and WSe<sub>2</sub> in their bulk state (top), after treatment with methylolithium (center) or butyllithium (bottom), with subsequent exfoliation in water. Scale bars represent 100 nm. White dotted arrows specify the direction parallel to sheets.

parent TMDs in comparison to their MeLi and BuLi exfoliated counterparts. In their bulk states, TMDs are observed as large polygonal stacks up to tens of micrometers across and thicknesses in the range of a few hundred nanometers. With subsequent treatment in MeLi, the average flake sizes of both tungsten dichalcogenides decreased, and WS<sub>2</sub> showed a noticeable representative expansion across its *c*-axis indicative of a successful intercalation. This was observed together with extensive wrinkling of the edges, likely formed as the result of the violent exfoliation process in water. MoSe<sub>2</sub> demonstrated a slight expansion of its layers but also some amount of exfoliation debris.

As may be expected, BuLi exfoliation was observed to be most effective across all materials, in contrast to MeLi, in line with its prior use in numerous chemical exfoliation procedures.<sup>2,3,25</sup> Although MoSe<sub>2</sub> and WS<sub>2</sub> showed greater wrinkling and expansion across their layers, individual layers do not clearly delaminate and can remain as stacked macrostructures. In addition for MoSe<sub>2</sub>, we determine the presence of surface oxides based on EDS (Supporting Information) and XPS data in the subsequent discussions. A more obvious delamination of layers was achieved using BuLi in the case of WSe<sub>2</sub>, where straight-cut edges were observed with minimal longitudinal breakage of the sheets.

Raman spectroscopy is then exploited as a valuable tool in obtaining structural evidence of the layered TMDs after exfoliation treatment. Figure 2 displays the Raman spectra of both bulk and treated TMDs, with peak data tabulated in Table S2. Typical spectra for all materials consist primarily of two characteristic peaks: the Raman active in-plane E<sup>1</sup><sub>2g</sub> and out-of-plane A<sub>1g</sub> modes, which we denote based on the D<sub>6h</sub> point group of the bulk material for consistency.<sup>26,27</sup>

Analysis of spectral characteristics for both vibrations consequently provides further information on their layered structures. While the in-plane E<sub>1g</sub> mode is also observed in all cases, its diagnostic value is comparatively limited.

First for MoSe<sub>2</sub>, we see no significant changes in the spectral features of the lines after treatment with MeLi, but notable differences with BuLi. Of note is the softening (4.6 cm<sup>-1</sup>) and broadening (0.7 cm<sup>-1</sup>) of the most intense A<sub>1g</sub> line, which is correlated to the edges of individual layers.<sup>28</sup> It is known that electron-doping results in our observed phenomena only for the A<sub>1g</sub> phonon and not the E<sup>1</sup><sub>2g</sub> phonon, which does not exhibit such a trend.<sup>29,30</sup> Hence, this confirms that electron donation from the C–Li bond to MoSe<sub>2</sub> had occurred with BuLi but not with MeLi.

Second for WS<sub>2</sub>, the broad trend observed is the lack of complete exfoliation of individual layers. An inspection of the E<sup>1</sup><sub>2g</sub> line reveals slight softening after treatment (2.3 cm<sup>-1</sup>), with a clear increase in its full-width at half-maximum (fwhm) from the bulk (9.0 cm<sup>-1</sup>) to the MeLi- (9.2 cm<sup>-1</sup>) and BuLi-treated (13.5 cm<sup>-1</sup>) materials, in agreement with earlier reports that the fwhm increases with a decreasing number of layers.<sup>31,32</sup> However, the same trend was not paralleled for the A<sub>1g</sub> line with no obvious changes in fwhm. More notable is the I<sub>A<sub>1g</sub></sub>/I<sub>E<sup>1</sup><sub>2g</sub></sub> ratio, which did not substantially decrease as is expected if exfoliation had proceeded to give three layers or less.<sup>33</sup> Thus, both SEM and Raman spectroscopy suggest that while some intercalation may have indeed occurred with both organolithium treatments, there is as yet little evidence to confirm complete delamination of individual WS<sub>2</sub> layers.

Finally in the case of WSe<sub>2</sub>, both E<sup>1</sup><sub>2g</sub> and A<sub>1g</sub> phonons are located in very close proximity at

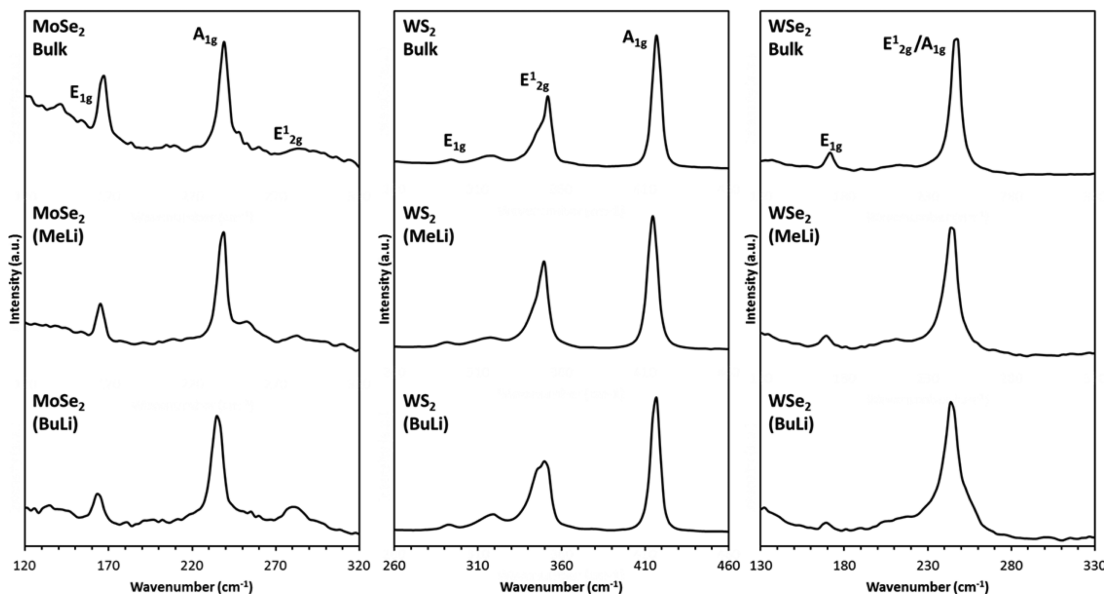


**Figure 2.** Raman spectra of MoSe<sub>2</sub>, WS<sub>2</sub>, and WSe<sub>2</sub> in their bulk state (top), after treatment with methyl lithium (center) or butyllithium (bottom), with subsequent exfoliation in water.  $\lambda_{\text{exc}} = 514.5 \text{ nm}$ .

ca. 250 and 253 cm<sup>-1</sup>.<sup>28</sup> A principal phenomenon indicative of exfoliation is the splitting of the overlapping peak that occurs for flakes of three layers or less, with the maximum 11 cm<sup>-1</sup> splitting for a monolayer.<sup>34</sup> In the instance with BuLi exfoliation, the broad shoulder peak centered 11 cm<sup>-1</sup> higher than the main peak signifies that monolayer WSe<sub>2</sub> was indeed obtained. It is very likely that this splitting is obscured from the superimposed spectra of other few-layered structures, resulting in the observed shoulder. Additionally, the softening of the main peak (4.7 cm<sup>-1</sup>) and its large increase in fwhm (3.3 cm<sup>-1</sup>) compared to the bulk material further prove that exfoliation was achieved for WSe<sub>2</sub>.

Even though insights were gained from microscopy and Raman spectroscopy, neither provides a truly quantifiable measure of exfoliation. Logically, the surface area is expected to increase after exfoliation, and it therefore serves as a good physical parameter to

determine the efficiency of exfoliation. Methylene blue adsorption has previously been employed for surface area determination of 2D layered materials such as graphenes,<sup>35–37</sup> and we now extend its application to include TMDs as a means to evaluate their exfoliation. As presented in Table 1, the measured surface area of each TMD is observed to increase considerably after MeLi treatment, but the highest values are obtained only with BuLi. Other key observations noted are that the most significant increase in surface area is for MoSe<sub>2</sub> after BuLi exfoliation, and both MeLi and BuLi resulted in similar exfoliation extents for WSe<sub>2</sub>. Even though small differences are noted in observations made between the three techniques, the overall conclusion remains that the BuLi exfoliation route is most effective, and different TMDs are seen to follow the order MoSe<sub>2</sub> > WS<sub>2</sub> > WSe<sub>2</sub>. Furthermore, the high surface area of BuLi-exfoliated MoSe<sub>2</sub> agrees well with colloidal MoSe<sub>2</sub> nanosheets determined using the BET method.<sup>20</sup>

To further understand the chemical changes associated with the structural transformations observed, we subsequently perform XPS to examine the surface elemental compositions and bonding information. We first study the bulk TMDs, and Figure 3 illustrates the high-resolution core-level Mo 3d and W 4f peaks. Deconvolution analysis of Mo bonding modes in bulk MoSe<sub>2</sub> shows a distinct pair of peaks (3d<sub>5/2</sub> and 3d<sub>3/2</sub>) originating primarily from the native semiconducting 2H phase in the IV oxidation state at ca. 229.5 and 232.5 eV,<sup>15,16,28,38,39</sup> with their atomic percentages

**TABLE 1.** Surface Area Measurements Based on Methylene Blue Adsorption on MoSe<sub>2</sub>, WS<sub>2</sub>, and WSe<sub>2</sub> in Solutions Prepared from Their Bulk States and after Treatment with Methylolithium or Butyllithium

material/treatment	MoSe <sub>2</sub>	WS <sub>2</sub>	WSe <sub>2</sub>	surface area (m <sup>2</sup> /g)
bulk	2.33	10.2	2.98	
MeLi-treated	33.8	13.9	24.5	
BuLi-treated	74.1	44.7	24.4	

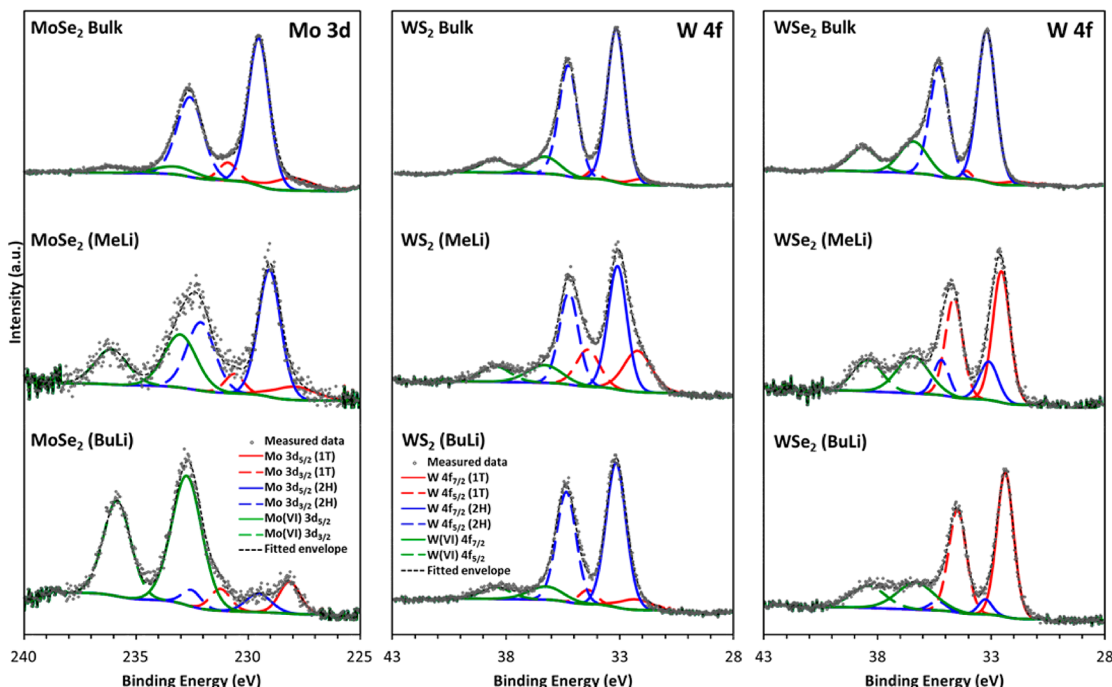


**Figure 3.** High-resolution X-ray photoelectron spectra of Mo 3d and W 4f regions of metal dichalcogenides in their bulk state (top), after treatment with methylolithium (center) or butyllithium (bottom), with subsequent exfoliation in water. Deconvoluted peaks correspond to the metallic 1T phase (red), semiconducting 2H phase (blue), or the oxidized (VI) state (green).

recorded in Table S3. Although XPS is an indispensable technique for analysis of TMD elemental compositions, it is also important to emphasize that intricate factors exist, such as the close proximities in binding energies of different phases.<sup>40</sup> Hence, the calculated atomic percentages reflect an overview of the relative changes in the materials as they undergo exfoliation, and individual values should not be interpreted as absolute quantities. In addition to the 2H phase, a small contribution of the 1T phase can also be found near 228.1 and 231.0 eV and a further pair from oxidized Mo(VI) species at approximately 232.7 and 235.8 eV. Similarly for the W 4f spectra of bulk WS<sub>2</sub> and WSe<sub>2</sub>, three pairs of peaks indicate the major presence of the 2H phase (~33.2 and 35.3 eV) and also the 1T phase (~32.1 and 34.4 eV) and W(VI) oxidation state (~36.3 and 38.5 eV) in lesser concentrations.<sup>28,32,41</sup> The 2H-polytype is dominant for all bulk TMDs at about 80 at. % and is surprisingly close to that for natural MoS<sub>2</sub> ore (molybdenite).<sup>42</sup> At this point, it is enlightening to note that small amounts of the transition metals exist in the oxidized VI state even for native bulk TMDs. Particularly, the increasing oxidation of bulk TMDs from MoSe<sub>2</sub> < WS<sub>2</sub> < WSe<sub>2</sub> agrees with reported trends that selenides are more easily oxidized than sulfides<sup>43</sup> and of tungsten over molybdenum dichalcogenides.<sup>44</sup>

Moving to investigate the effects of organolithium chemical exfoliation, the most striking observation is in MoSe<sub>2</sub>, showing a great increase in its Mo(VI) oxidation state with exfoliation. The presence of the oxidized VI species increases significantly after treatment with MeLi, up to a maximum of 78 at. % with BuLi. As the concentration of the 1T phase remains fairly constant at about 12 at. %, it is possible that electron doping of the original 2H phase *via* strong lithium-based reductants renders it unstable, leading to subsequent oxidation after atmospheric exposure. The surface Se/Mo atomic ratios were also seen to decrease considerably to only 0.7 after BuLi treatment, indicating a chalcogen-deficient surface. This observation was not replicated in other TMDs, which maintained their expected stoichiometric ratio of ~2 (Table S3). Moreover, both XPS and EDS (Tables S1 and S4) confirm a simultaneous increase in oxygen content. This trend is in direct opposition to the case of WS<sub>2</sub>, where no significant oxidation of the material was discovered. Also, no substantial conversion of the 2H to 1T phase was measured after treatment with BuLi, though a marginally larger 1T content was obtained with MeLi.

The disparity in exfoliation effects of the TMDs is most obvious for WSe<sub>2</sub>, as the only material showing a semblance of the 2H to 1T phase conversion known to occur in MoS<sub>2</sub> as a result of electron doping.<sup>16,25,45</sup> Peak deconvolution shows that the 1T percentage underwent a large increase from 2.6 at. % in the bulk to 66.7 at. % after exfoliation with BuLi. This conversion is seen from the experimental W 4f spectra, as denoted

by the gradual shift of the main peaks toward lower binding energies: with respect to the W(VI) 4f<sub>5/2</sub> peak with the highest energy at 38.5 eV, its separation from the main 4f<sub>5/2</sub> peak increases in the measured spectra from ~3.3 eV for bulk WSe<sub>2</sub> to 3.7 eV with MeLi treatment and 4.0 eV after BuLi treatment. On the basis of an earlier report,<sup>32</sup> we identify that a measured separation of 4.0 eV exists between the 4f<sub>5/2</sub> peaks of W(VI) and the 1T phase, while a smaller separation of ≤3.0 eV between the two 4f<sub>5/2</sub> peaks denotes the presence of a 2H phase. Overall, the observed 0.7 eV shift of the main peaks concurs with a previous report attributing it to a change in the surface doping.<sup>46</sup>

Hence, all evidence first reveals that the effectiveness of methylolithium is inferior to butyllithium as the classical reagent employed for TMD exfoliation. Both tungsten dichalcogenides show no significant changes in their chemical composition after BuLi treatment and demonstrate a substantial expansion of their *c*-axis, but stop short of attaining actual detachment of layers in WS<sub>2</sub>. MoSe<sub>2</sub> experienced the largest increase in surface area with BuLi exfoliation, but the treatment may have also resulted in its destabilization and consequent oxidation upon exposure to the environment.

**Differences in Inherent Electrochemistry of Molybdenum vs Tungsten Transition Metal Dichalcogenides.** The current achievements of MoS<sub>2</sub> as a viable catalyst for hydrogen evolution<sup>14–16</sup> and varied electrochemical applications<sup>11–13</sup> are simultaneously fueling the search for analogues among other layered TMD materials. Along with their proliferation as catalysts in electrochemistry, it is essential to acquire fundamental knowledge of their inherent electrochemical properties, which is not well studied at present. Also, the impact of the chemical exfoliation treatments on the TMDs is examined. Toward these ends, we carry out a systematic investigation of the TMDs using cyclic voltammetry as a suitable technique for examining the electrochemistry of layered materials such as graphenes<sup>47</sup> and TMDs.<sup>10,48</sup>

The voltammograms of all bulk and exfoliated TMDs are displayed in Figure 4, each characterized by their distinctive oxidation peaks. Of note is the incidence of varying peak shapes and positions, suggesting involvement of numerous species, which we subsequently attempt to identify. We can also reason that the inherent processes corresponding to these must involve chemically irreversible oxidations. This is particularly evidenced in MoSe<sub>2</sub> by the large peaks observed during the initial oxidative sweep and which virtually disappear from subsequent scans. However, for WS<sub>2</sub> and to a lesser extent in WSe<sub>2</sub>, these peaks significantly diminish in height after the first oxidative sweep, but broad peaks may still be observed even after two oxidation cycles. A further comparison with a previous report on MoS<sub>2</sub> shows that the recurrence of broad waves is a likely characteristic only of tungsten and not molybdenum dichalcogenides, highlighting

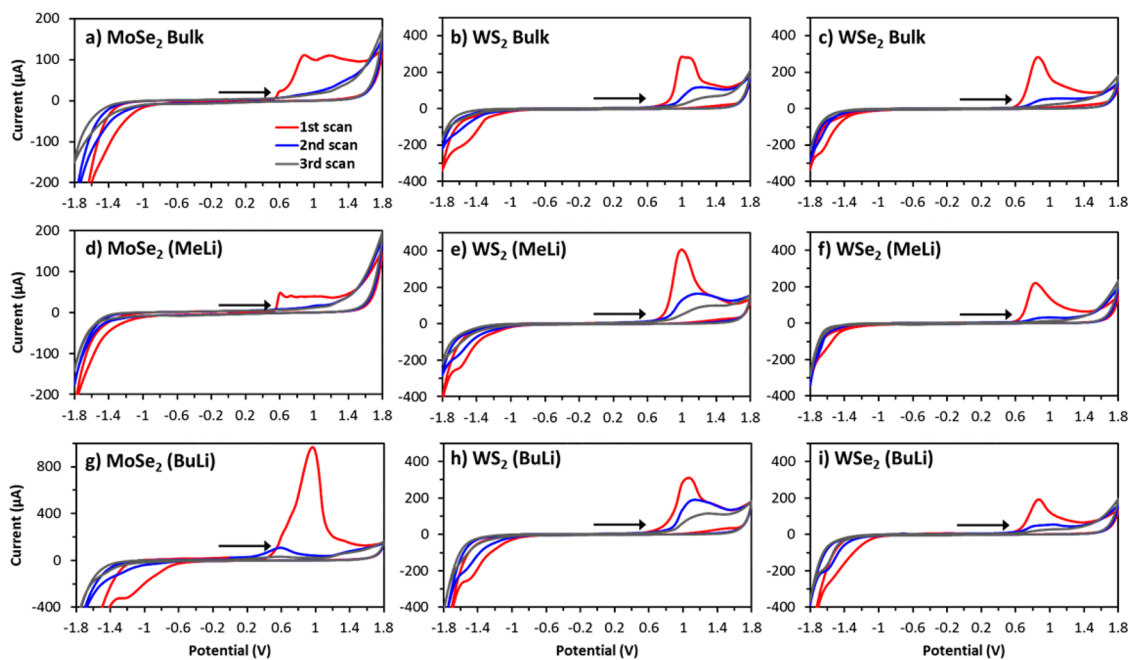


**Figure 4.** Cyclic voltammograms illustrating inherent electrochemistry of transition metal dichalcogenides in their bulk states (a–c) and as exfoliated in methyl lithium (d–f) and butyllithium (g–i). All scans start at 0.0 V vs Ag/AgCl, and arrows indicate the starting scan direction. First scans are labeled red, followed by second scans in blue and third scans in gray. Conditions: supporting electrolyte of 50 mM PBS at pH 7.2; scan rate: 100 mV s<sup>-1</sup>. Corresponding voltammograms with starting cathodic scans are available in the Supporting Information.

the possible difference in oxidation routes occurring between the two TMD elements.<sup>49</sup> It is also interesting to note an increase in oxidation potential in the order from WSe<sub>2</sub> < MoSe<sub>2</sub> < WS<sub>2</sub> < MoS<sub>2</sub>. These dissimilarities must again originate from the different reactants and products involved during electrochemical oxidation, and the solubility of their products can also play an important role.<sup>50</sup> One possibility resulting in this difference identified earlier from XPS is the larger presence of surface oxides in exfoliated MoSe<sub>2</sub> compared to similarly treated tungsten materials prior to any electrochemical treatment. Further XPS measurements after electro-oxidation confirm significant dissolution of MoSe<sub>2</sub> material (Figures S7 and S8) with a corresponding decrease in the Mo(VI) signal. Tungsten dichalcogenides in comparison maintain similar compositions after electro-oxidation. Hence, the soluble products formed from MoSe<sub>2</sub> electro-oxidation are immediately lost, but small amounts of insoluble oxides remain on tungsten TMD surfaces after electrochemical treatment. Examples could include tungsten oxide precipitates reported in WSe<sub>2</sub>.<sup>50</sup> These could subsequently detach gradually during potential cycling especially from hydrogen evolution induced at negative potentials and therefore appear as broad waves that decrease with each cycle. Considering the intrinsic HER catalytic activity of TMDs, it is also important to note possible delamination of surface material if strongly reducing potentials are applied.

We then scrutinize the significance of different peak potentials that occur for TMD electro-oxidations

depending on exfoliation treatment. MoSe<sub>2</sub> voltammetry is found to depend strongly on whether it exists as the bulk material, after MeLi treatment, or after exfoliation with BuLi. With only a few other reports on MoS<sub>2</sub> available,<sup>10,48,49</sup> very little else is known about the general inherent electrochemistry of TMDs. They however cite typical oxidation processes analogous to those observed in our voltammetry of MoSe<sub>2</sub>, WS<sub>2</sub>, and WSe<sub>2</sub>. In particular, two oxidation peaks were first reported by Chorkendorff *et al.*: a small peak at *ca.* 0.7 V and a notably larger peak at higher anodic potentials.<sup>48</sup> The two peaks were correlated to oxidation of the *edge* plane, which requires a lower overpotential and oxidation of the *basal* plane that necessitates application of a higher potential.<sup>50</sup> It then follows that peak potentials should increase after exfoliation in our case as more basal plane surfaces are revealed, which is indeed the trend observed for both tungsten dichalcogenides (Figure S5). The same general trend follows for MoSe<sub>2</sub> only for voltammetric runs started in the anodic direction, with the exception of an unusually low oxidation potential of the MeLi-treated product. Such a negative effect from MeLi treatment, however, can arise from the passivation and inactivation of TMD layers due to byproducts of the exfoliation reaction. The lithium intercalation mechanism is known to occur *via* a radical process, with lithium diffusion into the layers followed by combination of the corresponding radical moiety; the resulting butyl radical is observed to form octane as the final dimerization product in the BuLi case.<sup>2,51</sup> It stands to reason that MeLi treatment correspondingly

results in methyl radicals, but which are considerably more reactive and are known to attack oxides particularly prevalent in exfoliated MoSe<sub>2</sub>.<sup>52</sup> The higher carbon contents in all MeLi-treated materials measured from EDS and XPS (Tables S1 and S4) further support this proposition. Hence, the presence of more surface oxide in MoSe<sub>2</sub> inadvertently lends itself to passivation from MeLi.

This knowledge further explains differences in the oxidation potentials of MoSe<sub>2</sub> materials depending on whether an initial anodic or cathodic sweep was performed; higher peak potentials are seen from a starting anodic scan for both forms of exfoliated MoSe<sub>2</sub>, while the reverse is true for the bulk (Figure S5). We can reasonably infer from XPS that the initial reduction sweep causes surface oxides in MeLi- and BuLi-exfoliated MoSe<sub>2</sub> to undergo dissolution (Figure S7). This then reveals the original underlying MoSe<sub>2</sub> surface as validated by the position of the Se 3d<sub>5/2</sub> and 3d<sub>3/2</sub> peaks at 54 and 55 eV, respectively (Figure S8).<sup>28,39</sup> Subsequent reversal of the potential sweep toward the anodic direction then results in a peak at approximately 0.6 V and is thus likely to account for oxidation of MoSe<sub>2</sub> itself. This peak is always observed as a small prewave and also justifies the unusually low oxidation potential of the MeLi material with its passivated/inactive oxide surfaces. Instead, bulk MoSe<sub>2</sub> has at least three visible peaks at *ca.* 0.6, 0.8, and 1.2 V, of which the 1.2 V peak dominates if a cathodic sweep is performed first. Unlike its tungsten counterpart, the Se 3d peak of MoSe<sub>2</sub> appears at a higher binding energy after electro-oxidation, suggesting formation of a new selenium species that might explain this peak observed at high potential. Overall, the absence of such peculiar behavior in tungsten dichalcogenides again stems from the insolubility of its oxides and probable higher resistance to electro-oxidation.<sup>50</sup>

Despite the involvement of numerous convoluting aspects such as different electroactivities of edge vs basal planes, surface oxides, and their solubilities, a key interest remains in identifying the electrochemical redox processes responsible for the observations. We next perform voltammetry under similar conditions for both IV and VI oxides of molybdenum and tungsten (Figures S9, S10). Irreversible oxidation peaks are seen only for the IV oxides and not for the VI oxides. A sharp oxidation for molybdenum(IV) oxide is observed at 0.7 V close to those of MoSe<sub>2</sub>, whereas oxidation of tungsten(IV) oxide occurs at a slightly lower potential with a low and broad peak shape interestingly similar to tungsten dichalcogenides. These may serve as evidence for the proposed irreversible oxidation of metal centers from their +4 to +6 oxidation states<sup>48,49</sup> or otherwise as conclusive proof of oxide participation. Additional investigations show that a pH dependence of the oxidation peak (Figure S6) exists, but a linear correlation occurs only under acidic conditions ( $\text{pH} \leq 3$ ). Even so, the relation between oxidation potential and

pH does not equate to the 59 mV/pH value expected for a simple oxidation such as  $\text{WO}_2 + \text{H}_2\text{O} \rightarrow \text{WO}_3 + 2\text{H}^+ + 2\text{e}^-$ . The  $\text{H}^+:\text{e}^-$  ratios calculated for the observed oxidation peaks are  $\sim 1:16$ , 1:2, and 4:5 for MoSe<sub>2</sub>, WS<sub>2</sub>, and WS<sub>2</sub>, respectively. We may further postulate the identities of products based on thermodynamic stabilities at their observed potential. At strongly anodic potentials above  $\sim 1.0$  V vs Ag/AgCl, constituent elements would exist at their highest oxidation states and include both solid and aqueous species such as  $\text{MoO}_4^{2-}$ ,  $\text{WO}_3(\text{s})$ ,  $\text{HSO}_4^-$ , and  $\text{HSeO}_4^-$  under acidic conditions or  $\text{MoO}_4^{2-}$ ,  $\text{WO}_4^{2-}$ ,  $\text{SO}_4^{2-}$ , and  $\text{SeO}_4^{2-}$  at neutral to basic pH.<sup>50,53,54</sup> Hence, such a low proton:electron ratio especially for MoSe<sub>2</sub> is again suggestive of multiple processes involved, resulting in a combination of the above products.

Thus, far, we have shown that all the TMDs studied exhibit inherent electrochemistry, each bearing their specific set of characteristics. In addition to conventional wisdom on the effects of basal and edge planes,<sup>48–50</sup> we further propose that surface oxides can dictate the inherent electrochemistry of chemically exfoliated TMDs and are also influenced by their differing solubilities. Due to the greater solubility of oxides in MoSe<sub>2</sub>, more erratic behavior is observed, which we attribute to the redox reactions of MoSe<sub>2</sub> itself. Despite that their intricate redox mechanisms cannot be entirely elucidated at present, a more pressing concern for the immediate future is that inherent electrochemistry of TMDs can pose limitations on many related applications. One foremost constraint is the possible restriction of their operating potential windows as electrode materials in various fields such as sensing and electrocatalysis, which we study in depth next.

**Inherent Electrochemistry of TMDs Limits Potential Window of Common Redox Analytes.** In recent years, the majority of electrochemical applications involving TMDs are centered almost chiefly on HER catalysis. To address the relative shortfall in this aspect, we first explore the possibility of other potential applications such as ORR. Heterogeneous electron transfers at these surfaces are also investigated toward a redox analyte commonly used in electrochemical sensing. More importantly, effects and implications of the previously discussed inherent TMD electrochemistry are further studied in their contexts.

The heterogeneous electron transfer (HET) rate of an electrode material is a parameter of paramount importance and determines its suitability for electrochemical and biological sensing devices. An intrinsically fast HET rate is preferable for a prospective electrode material, as it effectively lowers the overpotential required for an electrochemical reaction. Cyclic voltammetry is first performed within the typical potential region for ferro/ferricyanide, as a redox couple commonly employed for electrochemical sensing purposes. HET rate constants are then calculated based on the

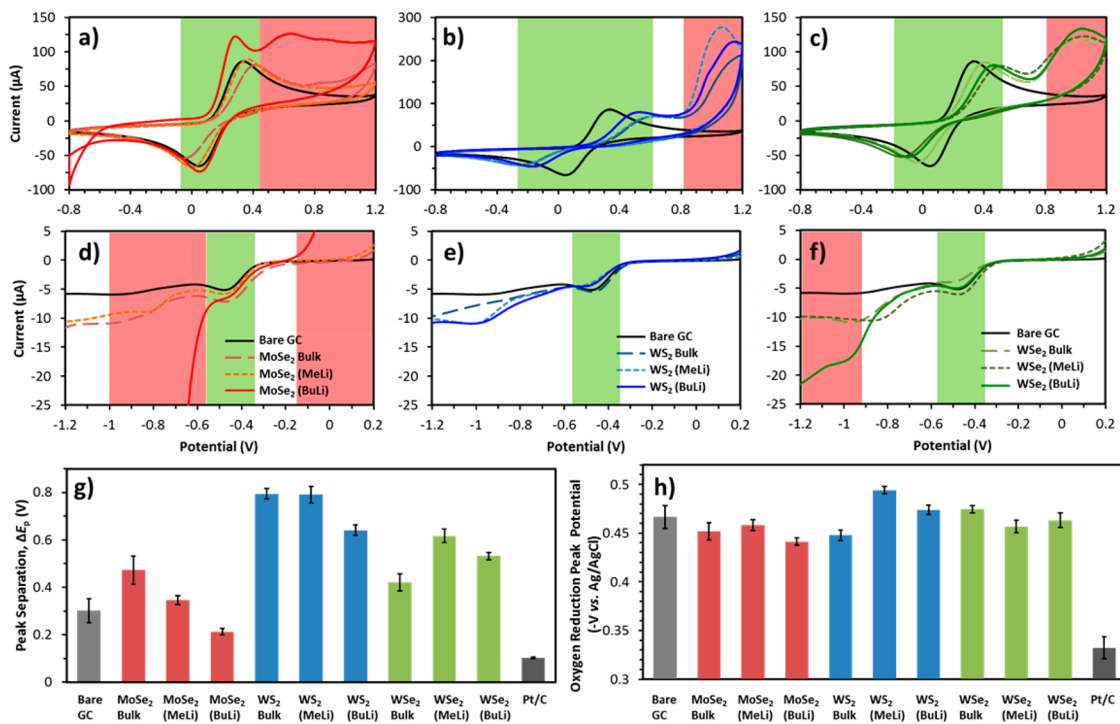


**Figure 5.** Electrochemical activities of the ferro/ferricyanide redox probe and the oxygen reduction reaction (ORR) on metal dichalcogenide catalysts. (a–c) Cyclic voltammograms for  $\text{Fe}(\text{CN})_6^{3-/4-}$  in 50 mM PBS supporting electrolyte at pH 7.2; scan rate: 100 mV s<sup>-1</sup>; only second scans are shown. (d–f) Oxygen reduction reaction on bulk and exfoliated  $\text{MoSe}_2$ ,  $\text{WS}_2$ , and  $\text{WSe}_2$ ; conditions: 0.1 M KOH; scan rate: 50 mV s<sup>-1</sup>. (g) Peak separations for the ferro/ferricyanide redox probe on TMD surfaces. (h) Peak reduction potentials for the ORR. Error bars correspond to standard deviations based on triplicate measurements. Green shaded regions designate the potential range where the analyte investigated is active, whereas red regions indicate the presence of inherent electroactivity from the TMD. Potentials are with respect to the Ag/AgCl reference electrode.

classical Nicholson approach,<sup>55</sup> with larger separations between the anodic and cathodic peaks relating to slower HET rates. A first observation in the voltammograms is that in addition to the reversible peaks of the ferro/ferricyanide couple appearing from -0.2 to 0.5 V vs Ag/AgCl, characteristic waves due to the inherent electrochemistry of the TMDs dominate their voltammetry particularly during the first scan (Figure S12) and occur at similar potentials as seen in the preceding section. Hence, immediate extraction of HET information from the initial scan cycle may be unreliable, and calculations are performed using data from the subsequent scans instead as shown in Figure 5a–c. Peaks from inherent TMD electroactivity are considerably diminished from the second scan onward, allowing for clear observation of the ferro/ferricyanide redox couple. Peak separations are presented in Figure 5g, from which the observed HET rate constants ( $k^0_{\text{obs}}$ ) are calculated (Table S6). Two distinct trends can be observed. The first is a dependence on the metal/chalcogen constituents of the TMDs irrespective of their chemical treatment, where  $\text{MoSe}_2$  typically exhibits the fastest HET and decreases in the order  $\text{MoSe}_2 > \text{WSe}_2 > \text{WS}_2$ . It is unsurprising that this trend is found to correspond to their electrical conductivities (Figure S13), as the intrinsic conductivity is a foremost determinant of the observed HET at an electrode surface. On one

extreme, all  $\text{WS}_2$  materials showed irreversible  $k^0_{\text{obs}}$  values lower than the quasi-reversible limit, which we determine to be  $6.3 \times 10^{-6} \text{ cm s}^{-1}$  at the scan rate used,<sup>56</sup> and are thus unsuitable for electrochemical sensing. On the other hand, BuLi-exfoliated  $\text{MoSe}_2$  has the highest  $k^0_{\text{obs}}$  value of  $9.17 \times 10^{-4} \text{ cm s}^{-1}$ , better than that of conventional GC electrodes at  $2.78 \times 10^{-4} \text{ cm s}^{-1}$ . This leads to the observation of the exfoliation method as a secondary factor influencing HET rate. Materials demonstrated improved HET rates after BuLi exfoliation compared to their MeLi-treated counterparts, followed by the bulk materials with the slight exception of bulk  $\text{WSe}_2$ . Such an improvement in HET may be correlated with the increase in surface area as a direct consequence of the exfoliation process as shown earlier. Overall, combined effects of a high conductivity and increased surface area result in BuLi-exfoliated  $\text{MoSe}_2$  exhibiting the fastest HET rate.

We subsequently turn our attention to the oxygen reduction reaction with its key importance in fuel cell technologies.<sup>57</sup> Two reduction peaks near -0.4 and -0.9 V vs Ag/AgCl corresponding to the two-step reduction process of  $\text{O}_2$  are observed. In addition to the appearance of inherent oxidation waves at positive potentials, we now also note the incidence of inherent reduction peaks, especially in BuLi-exfoliated  $\text{MoSe}_2$  and  $\text{WSe}_2$  within the potentials highlighted in red

(ca.  $-0.8$  V to  $-1.0$  V) in Figure 5d and f. Closer examination of the inherent reductions (Figure S14) reveals a sharp faradaic process for MoSe<sub>2</sub> and a drawn out wave in the case of WSe<sub>2</sub> but altogether not in WS<sub>2</sub>, allowing us to deduce that these inherent reductions must involve selenides, likely in forming compounds such as HSe<sup>-</sup> based on the potentials in which they occur.<sup>53,54</sup>

For the purposes of studying the electrocatalysis of oxygen reduction, we focus only on the reduction peak at about  $-0.4$  V vs Ag/AgCl corresponding to the first two-electron reduction step. As collated in Figure 5h, the lowest reduction peak potential occurs for Pt/C at about  $-0.33$  V vs Ag/AgCl, agreeing with the use of Pt-based catalysts as the current state-of-the-art in proton exchange membrane fuel cells.<sup>57</sup> Unlike the case of ferro/ferricyanide catalysis, neither TMD compositions nor the chemical exfoliation methods have any obvious effect on ORR, and MoSe<sub>2</sub> materials ( $-0.44$ ,  $-0.45$ , and  $-0.46$  V for BuLi-exfoliated, bulk, and MeLi-treated MoSe<sub>2</sub>, respectively) show just a marginal improvement in their reduction peak potentials from GC electrodes at  $-0.47$  V likely due to their higher intrinsic conductivities. No other relation is discernible, specifically within tungsten dichalcogenides. As such, the only factor for enhancement of ORR catalysis in TMDs currently known is that of size effects.<sup>58</sup>

We can thus conclude that there is a strong dependence of TMD compositions and the choice of chemical exfoliation method on ferro/ferricyanide catalysis due to differences in electrical conductivity and surface area, but such effects are less distinct for the ORR. In addition, inherent electrochemistry characteristics of the various TMDs are shown to occur within both anodic and cathodic potentials of  $\pm 1.2$  V for common analytes (ferrocyanide and aqueous dissolved oxygen) as model systems. Inherent TMD electroactivities within the same potential window of an analyte may limit applications if caution is not exercised, especially if there is a lack of controls to distinguish analyte from inherent electrode activity. Therefore, these new insights can effectively provide recourse to the future use of TMDs in sensing and catalysis applications.

**Hydrogen Evolution Reaction: Strong Dependence on Metal/Chalcogen Composition and Exfoliation Method.** In stark contrast to the ORR, the HER efficiency is seen to have strong dependencies on the chemical exfoliation route and TMD composition. Linear sweep HER measurements were performed in N<sub>2</sub>-saturated 0.5 M sulfuric acid at a low scan rate of 2 mV s<sup>-1</sup> for bulk and exfoliated TMDs, with their polarization curves shown in Figure 6a–c. Polarization curves for bare GC electrodes and finely dispersed platinum-on-carbon as the best known HER electrocatalyst are also demonstrated for reference. We observe the lowest onset potential of approximately  $-0.13$  V vs RHE for MoSe<sub>2</sub> after BuLi

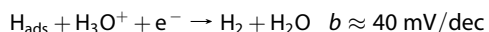
treatment against a significantly poorer  $-0.29$  V vs RHE for the bulk material. This low onset potential is very similar to that recently reported for MoSe<sub>2</sub> nanosheets<sup>39</sup> and also for MoS<sub>2</sub> nanoparticles.<sup>15</sup> For a tenable evaluation of catalytic performance across the literature, however, the overpotential at a current density of 10 mA cm<sup>-2</sup> is used instead. At this increased level of H<sub>2</sub> production, a comparison of the overpotential between different TMDs (Figure 6f) reveals a first trend: MoSe<sub>2</sub> materials always performed best followed by WS<sub>2</sub> and WSe<sub>2</sub>. Interestingly, there is also a second dependence on the choice of chemical intercalant used; BuLi-exfoliated catalysts always showed an improvement from the bulk, while MeLi treatment of the TMDs results in poorer catalysis. Overall, BuLi-exfoliated MoSe<sub>2</sub> was the most efficient HER catalyst ( $-0.36$  V vs RHE) followed by the unexfoliated bulk ( $-0.53$  V) and MeLi-treated MoSe<sub>2</sub> ( $-0.66$  V) at greater reducing overpotentials. It is much expected that the HER efficiency increases after BuLi treatment due to the concomitant effects of (1) an abundance of active edge sites from the exfoliation of layers,<sup>14,59</sup> (2) phase transition to the more catalytic 1T polymorph due to electron transfer from the C–Li bond in butyllithium,<sup>16,25</sup> and (3) a reduction in the potential barrier for electron hopping with a decreasing number of layers.<sup>38</sup> In terms of more convenient parameters, this enhancement in HER efficiency is clearly correlated with BuLi exfoliation due to the surface area increase determined earlier. With MeLi, however, any effect from increased surface area is effectively negated by passivation of TMD surfaces from reactive methyl radicals,<sup>52</sup> mirroring our observations in their inherent electrochemistry. This is also reflected in their typically lower conductivity values (Figure S13).

Tafel analysis was subsequently executed for the HER polarization curves to elucidate the electrochemical mechanisms (Figure 6d), with their values tabulated in Figure 6e. The mechanism of the hydrogen evolution on different TMD surfaces can be understood from the rate-determining steps as such:<sup>15</sup>

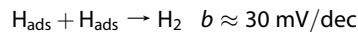
1. Volmer adsorption step:



2. Heyrovsky desorption step:



3. Tafel desorption step:



In the widely studied MoS<sub>2</sub> analogue, both the metallic 1T phase and active edge sites are known to be electrocatalytic for HER, with prior reports showing the lowest Tafel slopes for metallic MoS<sub>2</sub> at typically  $\sim 40$  mV/dec,<sup>16,25</sup> agreeing with the Volmer–Heyrovsky mechanism. In comparison, edge-rich nanosheets show a slightly higher Tafel slope of 55–60 mV/dec.<sup>14</sup>

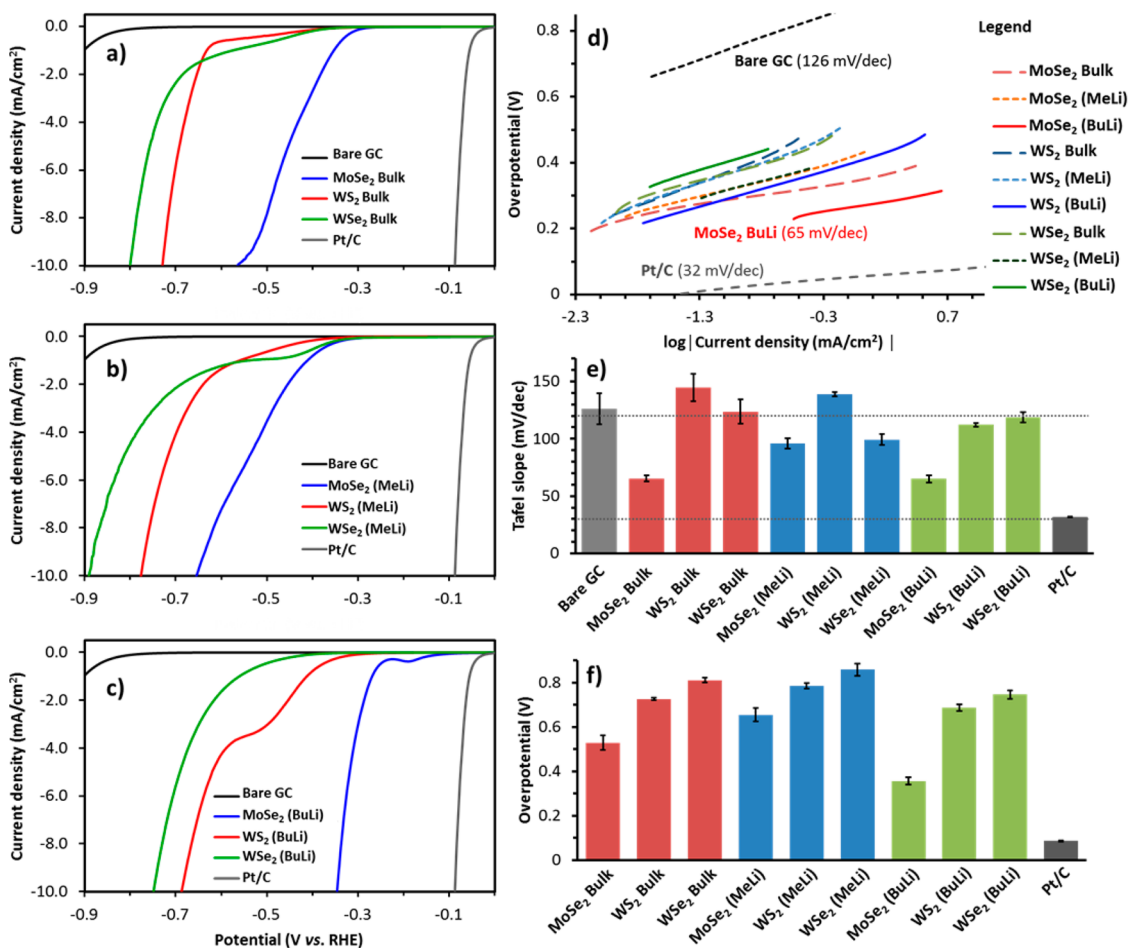


**Figure 6.** Electrochemical activity of the hydrogen evolution reaction (HER) on metal dichalcogenide catalysts. Polarization curves (a–c) for HER on bulk and exfoliated MoSe<sub>2</sub>, WS<sub>2</sub>, and WSe<sub>2</sub>. Bare glassy carbon electrodes and platinum on carbon catalyst are also shown for comparison. Conditions: 0.5 M H<sub>2</sub>SO<sub>4</sub>; scan rate: 2 mV s<sup>-1</sup>. (d) Tafel plot for the HER. (e) Tabulated values for the Tafel slope; dotted lines at 120 and 30 mV/dec correspond to the Volmer and Tafel mechanisms, respectively. (f) Overpotentials required for the HER at 10 mA cm<sup>-2</sup> current density. Error bars correspond to standard deviations based on triplicate measurements.

We observe in our case a Tafel slope of 126 mV/dec on bare GC electrodes, indicating adsorption as the slow step in contrast to the most catalytic Pt/C with a value of 32 mV/dec corresponding to the Tafel reaction. The broad trend we observed for both tungsten dichalcogenides is the Volmer adsorption mechanism as the limiting step with slopes generally close to its 120 mV/dec theoretical value.

The highest catalytic efficiencies however were consistently seen in MoSe<sub>2</sub>, with Tafel slopes ranging significantly lower at an average of ~65 mV/dec for the bulk and also after BuLi exfoliation, whereas a 96 mV/dec value was obtained for the MeLi-treated material. Since experimental Tafel slopes are a direct outcome of surface HER mechanisms, it is thus prudent to consider surface compositions of the catalysts. Constituent elements of the TMDs themselves may first contribute to their varying HER performance, in addition to possible negative effects of insoluble surface oxides from tungsten dichalcogenides. Though this is deterministic of different TMDs, the surface metal-to-chalcogen ratios

instead represent a potential point of control in improving HER efficiency. We see from XPS that only MoSe<sub>2</sub> materials exhibit chalcogen-deficient surfaces (Table S3). Their surface compositions are MoSe<sub>(2-x)</sub>, where  $x = 0.6$  and  $0.7$  for bulk and MeLi-treated MoSe<sub>2</sub>, respectively, with the BuLi-treated material being most deficient in selenium at  $x = 1.3$ . This is in agreement with Mo edge sites shown to have a lower energy barrier for hydrogen evolution in Mo<sub>2</sub>,<sup>48,60</sup> MoSe<sub>2</sub>,<sup>61</sup> and also experimentally shown with colloidal MoSe<sub>2</sub> having unsaturated Se-edges<sup>62</sup> and vacancies.<sup>20</sup> The chalcogen deficiency in our case is likely to have arisen from surface oxidation shown previously from XPS and SEM-EDS and intriguingly enhances the overpotential and Tafel slope. Again, the poorer slope after MeLi treatment supports our proposition of surface passivation by methyl radicals. Overall, the 65 mV/dec value that we see for exfoliated MoSe<sub>2</sub> is improved from that of pure MoSe<sub>2</sub> nanosheets at 101 mV/dec<sup>39</sup> and free MoS<sub>2</sub> nanoparticles at 94 mV/dec.<sup>15</sup> Thus, HER efficiencies of TMDs are observed to be profoundly dependent on the metal-to-chalcogen

composition, which determines the intrinsic free energy for adsorption of atomic hydrogen, and also the exfoliation method employed, which in turn influences the catalytic edge sites and polymorphs.

Another point of interest is the presence of prewaves seen only in some materials such as MoSe<sub>2</sub> and WS<sub>2</sub> after BuLi exfoliation. To this, there are two possibilities stemming from either intrinsic chemical or physical processes; first is the inherent TMD electroactivity as outlined previously, while the second is varying catalytic efficiencies of HER on different sites such as edge and basal planes. Chemically irreversible reductions were observed only in some materials, noted by their disappearance after the initial HER measurement with no apparent effects on the subsequent HER efficiency (Figure S17). However, the charges passed within these HER prewaves do not necessarily correspond with the charges measured from inherent reductions and are usually far greater by about 2 orders of magnitude (Figure S18). Therefore, while the inherent electrochemistry of the TMDs is a probable cause of HER prewaves wherever they arise, differences in catalytic activities of TMD surfaces may also be an important contributing factor,<sup>14</sup> such as the enhanced catalysis at edge sites against basal planes with their sluggish kinetics. Nonetheless as we have shown, the effects of TMD composition and exfoliation method can still be accurately investigated by evaluating materials at a suitably high current density to avoid misinterpretation from inherent electroactivity. This substantiates our notion that accurate information can be obtained only with a good understanding of fundamental TMD properties.

## CONCLUSION

We have performed a comprehensive investigation into the effects of chemical exfoliation of TMDs (MoSe<sub>2</sub>, WS<sub>2</sub>, WSe<sub>2</sub>) and extensively examined their properties toward a variety of electrochemical aspects and applications. Strong dependences on the TMD composition and chemical exfoliation route are found to exist due to changes in properties such as surface area and electrical conductivity. All TMDs investigated possess inherent electrochemical activity, and their characteristics are influenced by their compositions, with molybdenum exhibiting greater variation over tungsten TMDs. Inherent electroactivities can pose limitations for their current use as electrocatalysts and also electrode materials in other applications. Voltammetric studies reveal that possible complications may arise in many areas such as sensing and catalysis, even for common redox reactions within a relatively small potential window of  $\pm 1$  V and over a wide range of pH. In summary, care must be taken when exploiting TMD materials for any electrochemical purpose, as activity of the electrode material itself may convolute data obtained and result in erroneous interpretations. Therefore, an awareness of TMD electrochemistry is especially crucial for the current development of HER catalysts and useful outcomes may nevertheless be achieved with proper application of this new knowledge. We prove this to be true in electrochemical sensing where heterogeneous electron transfer rates can be accurately determined at TMD surfaces and also in HER catalysis where highly efficient hydrogen production can be accomplished by the careful choice of TMD composition and exfoliation routes.

## METHODS

Molybdenum selenide (99.9%), tungsten sulfide (99.8%), and tungsten selenide (99.8%) were obtained from Alfa Aesar (Germany). Methylolithium (1.6 M in diethyl ether), *n*-butyllithium (1.6 M in hexane), and methylene blue were obtained from Sigma-Aldrich, Czech Republic. Hexane was obtained from Lach-ner, Czech Republic. Concentrated sulfuric acid, potassium hydroxide, dibasic potassium phosphate, monobasic sodium phosphate, sodium chloride, potassium chloride, potassium ferrocyanide, 20 wt % platinum on graphitized carbon (Pt/C), and all transition metal oxides were obtained from Sigma-Aldrich (Singapore). Glassy carbon (GC) electrodes and a platinum electrode (Pt) purchased from CH Instruments (Austin, TX, USA) of 3 mm diameters were used as working and auxiliary electrodes, respectively. A Ag/AgCl (1 M KCl) electrode was used as the reference. Deionized water with a resistivity of 18.2 M $\Omega$  cm was used throughout in the preparation of solutions.

The exfoliation of TMDs was carried out by suspension of 15 mmol of a particular TMD bulk powder in 20 mL of 1.6 M methylolithium in diethyl ether and 20 mL of 1.6 M *n*-butyllithium in hexane. The solution is then stirred for 72 h at 25 °C under an argon atmosphere. The Li-intercalated material is separated by suction filtration under an argon atmosphere, and the intercalation compound was washed several times with hexane (dried over Na). The separated TMD with intercalated Li was

subsequently placed in water (100 mL) and repeatedly centrifuged (18000g). The final obtained materials were dried in a vacuum oven at 50 °C for 48 h prior to further use.

Scanning electron microscopy was done using a JEOL 7600F field-emission scanning electron microscope (JEOL, Japan) in gentle-beam mode at 2 kV. Energy dispersive X-ray spectroscopy data were obtained at an accelerating voltage of 15 kV. Raman spectroscopy was performed on a confocal micro-Raman LabRam HR instrument (Horiba Scientific) in backscattering geometry with a CCD detector, with a 514.5 nm argon-ion excitation laser and a 100 $\times$  objective mounted on an Olympus optical microscope. The laser spot size was approximately 5  $\mu$ m across. Instrument calibration was achieved with a silicon reference giving a peak position at 520 cm<sup>-1</sup>. Samples were prepared by drop-casting ultrasonicated dispersions with a concentration of 1.0 mg mL<sup>-1</sup> in deionized water onto a silicon wafer. X-ray photoelectron spectroscopy was performed with a Phoibos 100 spectrometer with a Mg K $\alpha$  X-ray source (SPECS, Germany) at 1254 eV. Relative sensitivity factors were used for evaluation of chalcogen-to-metal ratios and quantitative distributions of 2H and 1T phases and the oxidation states in Mo and W. Electrochemical analyses were performed in a 5 mL electrochemical cell at room temperature using a standard three-electrode configuration on an Autolab PGSTAT 101 electrochemical analyzer (Eco Chemie, Utrecht, The Netherlands) controlled by NOVA version 1.8 software (Eco Chemie). Surface areas were measured

using adsorption of methylene blue. About 0.1 g of each TMD material (weighed exactly to within  $\pm 0.01$  mg) was dispersed in 70 mL of deionized water by ultrasonication (400 W, 30 min). To the suspension was added 1 mM aqueous solution of methylene blue and then filled to 100 mL. Concentration of unabsorbed methylene blue was determined by UV-vis spectroscopy at  $\lambda_{\text{max}} = 665$  nm (Cary 50, Agilent). For the calculation of surface areas, the value of  $1.3 \text{ nm}^2$  per methylene blue molecule was used.<sup>35</sup>

Aqueous dispersions of transition metal dichalcogenide catalysts were first prepared in deionized water at a  $1.0 \text{ mg mL}^{-1}$  concentration with ultrasonication for 1 h to obtain a well-dispersed suspension. The dispersion process was most efficient for butyllithium-exfoliated materials, as indicated by the intense change of solution color, which continued to remain stable after just  $\sim 15$  min of sonication. Bulk materials require longer periods of more than 40–50 min, with only slight increase in color intensities. Suspensions of bulk TMDs are unstable, and agglomeration is almost immediate. Aliquots of  $5 \mu\text{L}$  of the dispersion inks were then drop-casted on GC electrodes immediately after sonication and dried, giving a catalyst loading of  $70.7 \mu\text{g cm}^{-2}$  per electrode. GC electrode surfaces were renewed prior to new measurements by polishing with a  $0.05 \mu\text{m}$  alumina particle slurry on a polishing pad and thoroughly washed with deionized water.

Studies on the inherent electrochemistry of TMDs on modified electrodes were made in a 50 mM phosphate-buffered saline (PBS, pH 7.2) solution using cyclic voltammetry at a scan rate of  $100 \text{ mV s}^{-1}$ . The hydrogen evolution reaction was investigated by linear sweep voltammetry in 0.5 M  $\text{H}_2\text{SO}_4$  at a scan rate of  $2 \text{ mV s}^{-1}$ . Measurements of the heterogeneous electron transfer rates at TMD surfaces were done using PBS as the supporting electrolyte for 10 mM of the ferro/ferricyanide redox probe. Cyclic voltammetry experiments were performed at a fixed scan rate of  $100 \text{ mV s}^{-1}$ , and only data from second scans were used to avoid interferences arising from inherent peaks occurring in the initial scan. Solutions were purged with nitrogen gas before measurements. Calculation for the HET rate constant ( $k^0_{\text{obs}}$ ) was achieved using the method developed by Nicholson,<sup>55</sup> relating the observed  $\Delta E_p$  to a dimensionless parameter,  $\psi$ , and consequently to  $k^0_{\text{obs}}$ . The roughness factor was not taken into account in this case. The  $[\text{Fe}(\text{CN})_6]^{3-}/4-$  diffusion coefficient of  $7.26 \times 10^{-6} \text{ cm}^2 \text{ s}^{-1}$  was used for calculation.<sup>63</sup> Calculation of the quasi-reversible limits for  $k^0_{\text{obs}}$  is based on the definition by Matsuda and Ayabe.<sup>56</sup> Voltammetric measurements of the oxygen reduction reaction on TMDs were also obtained in an oxygen-saturated solution of 0.1 M KOH achieved by bubbling. A scan rate of  $50 \text{ mV s}^{-1}$  was used.

**Conflict of Interest:** The authors declare no competing financial interest.

**Supporting Information Available:** Elemental mappings from energy-dispersive X-ray spectroscopy and their atomic composition values; tabulated peak data from Raman spectroscopy; wide-scan and high resolution X-ray photoelectron spectra with deconvolution data; elemental atomic compositions based on XPS; cyclic voltammograms illustrating inherent electroactivity of TMDs and its pH dependence; XPS analysis of TMDs after electrochemical treatment; characteristic electrochemical behaviors of related oxides and compounds; tabulated heterogeneous electron transfer rate constants for ferro/ferricyanide on TMD surfaces; voltammograms illustrating inherent electroactivities during ferrocyanide sensing or the oxygen reduction and hydrogen evolution reactions under specific conditions; electrical conductivities of TMDs on interdigitated electrodes. This material is available free of charge via the Internet at <http://pubs.acs.org>.

**Acknowledgment.** M.P. acknowledges Tier 2 grant (MOE2013-T2-1-056; ARC 35/13) from the Ministry of Education, Singapore. Z.S. was supported by Specific University Research (MSMT no. 20/2014). M.P. and A.Y.S.E. designed the research; A.Y.S.E., A.A., and Z.S. performed the experiments; A.Y.S.E., A.A., and Z.S. analyzed the data; Z.S. and P.S. performed the synthetic procedures; A.Y.S.E. and M.P. wrote the manuscript.

## REFERENCES AND NOTES

- Sebenik, R. F.; Burklin, A. R.; Dorfler, R. R.; Laferty, J. M.; Leichtfried, G.; Meyer-Grönnow, H.; Mitchell, P. C. H.; Vukasovich, M. S.; Church, D. A.; Van Riper, G. G.; et al. Molybdenum and Molybdenum Compounds. In *Ullmann's Encyclopedia of Industrial Chemistry*; Ullmann, F., Ed.; Wiley-VCH: Weinheim, 2000; p 523.
- Dines, M. B. Lithium Intercalation via n-Butyllithium of the Layered Transition Metal Dichalcogenides. *Mater. Res. Bull.* **1975**, *10*, 287–291.
- Whittingham, M. S.; Gamble, F. R., Jr. The Lithium Intercalates of the Transition Metal Dichalcogenides. *Mater. Res. Bull.* **1975**, *10*, 363–371.
- Coleman, J. N.; Lotya, M.; O'Neill, A.; Bergin, S. D.; King, P. J.; Khan, U.; Young, K.; Gaucher, A.; De, S.; Smith, R. J.; et al. Two-Dimensional Nanosheets Produced by Liquid Exfoliation of Layered Materials. *Science* **2011**, *331*, 568–571.
- Chhowalla, M.; Shin, H. S.; Eda, G.; Li, L.-J.; Loh, K. P.; Zhang, H. The Chemistry of Two-Dimensional Layered Transition Metal Dichalcogenide Nanosheets. *Nat. Chem.* **2013**, *5*, 263–275.
- Pumera, M.; Sofer, Z.; Ambrosi, A. Layered Transition Metal Dichalcogenides for Electrochemical Energy Generation and Storage. *J. Mater. Chem. A* **2014**, *2*, 8981–8987.
- Gao, M.-R.; Xu, Y.-F.; Jiang, J.; Yu, S.-H. Nanostructured Metal Chalcogenides: Synthesis, Modification, and Applications in Energy Conversion and Storage Devices. *Chem. Soc. Rev.* **2013**, *42*, 2986–3017.
- Roome, N. J.; Carey, J. D. Beyond Graphene: Stable Elemental Monolayers of Silicene and Germanene. *ACS Appl. Mater. Interfaces* **2014**, *6*, 7743–7750.
- Xu, M.; Liang, T.; Shi, M.; Chen, H. Graphene-Like Two-Dimensional Materials. *Chem. Rev.* **2013**, *113*, 3766–3798.
- Wu, S.; Zeng, Z.; He, Q.; Wang, Z.; Wang, S. J.; Du, Y.; Yin, Z.; Sun, X.; Chen, W.; Zhang, H. Electrochemically Reduced Single-Layer MoS<sub>2</sub> Nanosheets: Characterization, Properties, and Sensing Applications. *Small* **2012**, *8*, 2264–2270.
- Chen, D.; Ji, G.; Ding, B.; Ma, Y.; Qu, B.; Chen, W.; Lee, J. Y. *In Situ* Nitrogenated Graphene–Few-Layer WS<sub>2</sub> Composites for Fast and Reversible Li<sup>+</sup> Storage. *Nanoscale* **2013**, *5*, 7890–7896.
- Cao, L.; Yang, S.; Gao, W.; Liu, Z.; Gong, Y.; Ma, L.; Shi, G.; Lei, S.; Zhang, Y.; Zhang, S.; et al. Direct Laser-Patterned Micro-Supercapacitors from Paintable MoS<sub>2</sub> Films. *Small* **2013**, *9*, 2905–2910.
- Bernardi, M.; Palummo, M.; Grossman, J. C. Extraordinary Sunlight Absorption and One Nanometer Thick Photovoltaics Using Two-Dimensional Monolayer Materials. *Nano Lett.* **2013**, *13*, 3664–3670.
- Jaramillo, T. F.; Jørgensen, K. P.; Bonde, J.; Nielsen, J. H.; Horch, S.; Chorkendorff, I. Identification of Active Edge Sites for Electrochemical H<sub>2</sub> Evolution from MoS<sub>2</sub> Nanocatalysts. *Science* **2007**, *317*, 100–102.
- Li, Y.; Wang, H.; Xie, L.; Liang, Y.; Hong, G.; Dai, H. MoS<sub>2</sub> Nanoparticles Grown on Graphene: An Advanced Catalyst for the Hydrogen Evolution Reaction. *J. Am. Chem. Soc.* **2011**, *133*, 7296–7299.
- Voiry, D.; Salehi, M.; Silva, R.; Fujita, T.; Chen, M.; Asefa, T.; Shenoy, V. B.; Eda, G.; Chhowalla, M. Conducting MoS<sub>2</sub> Nanosheets as Catalysts for Hydrogen Evolution Reaction. *Nano Lett.* **2013**, *13*, 6222–6227.
- Wang, H.; Lu, Z.; Xu, S.; Kong, D.; Cha, J. J.; Zheng, G.; Hsu, P.-C.; Yan, K.; Bradshaw, D.; Prinz, F. B.; et al. Electrochemical Tuning of Vertically Aligned MoS<sub>2</sub> Nanofilms and its Application in Improving Hydrogen Evolution Reaction. *Proc. Natl. Acad. Sci. U.S.A.* **2013**, *110*, 19701–19706.
- Zhou, K.-G.; Mao, N.-N.; Wang, H.-X.; Peng, Y.; Zhang, H.-L. A Mixed-Solvent Strategy for Efficient Exfoliation of Inorganic Graphene Analogues. *Angew. Chem., Int. Ed.* **2011**, *50*, 10839–10842.
- Mahler, B.; Hoepfner, V.; Liao, K.; Ozin, G. A. Colloidal Synthesis of 1T-WS<sub>2</sub> and 2H-WS<sub>2</sub> Nanosheets: Applications for Photocatalytic Hydrogen Evolution. *J. Am. Chem. Soc.* **2014**, *136*, 14121–14127.

20. Zhou, X.; Jiang, J.; Ding, T.; Zhang, J.; Pan, B.; Zuo, J.; Yang, Q. Fast Colloidal Synthesis of Scalable Mo-Rich Hierarchical Ultrathin  $\text{MoSe}_{2-x}$  Nanosheets for High-Performance Hydrogen Evolution. *Nanoscale* **2014**, *6*, 11046–11051.
21. Li, H.; Wu, J.; Yin, Z.; Zhang, H. Preparation and Applications of Mechanically Exfoliated Single-Layer and Multilayer  $\text{MoS}_2$  and  $\text{WSe}_2$  Nanosheets. *Acc. Chem. Res.* **2014**, *47*, 1067–1075.
22. Novoselov, K. S.; Jiang, D.; Schedin, F.; Booth, T. J.; Khotkevich, V. V.; Morozov, S. V.; Geim, A. K. Two-Dimensional Atomic Crystals. *Proc. Natl. Acad. Sci. U.S.A.* **2005**, *102*, 10451–10453.
23. Lee, Y.-H.; Zhang, X.-Q.; Zhang, W.; Chang, M.-T.; Lin, C.-T.; Chang, K.-D.; Yu, Y.-C.; Wang, J. T.-W.; Chang, C.-S.; Li, L.-J.; et al. Synthesis of Large-Area  $\text{MoS}_2$  Atomic Layers with Chemical Vapor Deposition. *Adv. Mater.* **2012**, *24*, 2320–2325.
24. Wang, S.; Rong, Y.; Fan, Y.; Pacios, M.; Bhaskaran, H.; He, K.; Warner, J. H. Shape Evolution of Monolayer  $\text{MoS}_2$  Crystals Grown by Chemical Vapor Deposition. *Chem. Mater.* **2014**, *26*, 6371–6379.
25. Lukowski, M. A.; Daniel, A. S.; Meng, F.; Forticaux, A.; Li, L.; Jin, S. Enhanced Hydrogen Evolution Catalysis from Chemically Exfoliated Metallic  $\text{MoS}_2$  Nanosheets. *J. Am. Chem. Soc.* **2013**, *135*, 10274–10277.
26. Tonndorf, P.; Schmidt, R.; Böttger, P.; Zhang, X.; Börner, J.; Liebig, A.; Albrecht, M.; Kloc, C.; Gordan, O.; Zahn, D. R. T.; et al. Photoluminescence Emission and Raman Response of Monolayer  $\text{MoS}_2$ ,  $\text{MoSe}_2$  and  $\text{WSe}_2$ . *Opt. Express* **2013**, *21*, 4908–4916.
27. Terrones, H.; Del Corro, E.; Feng, S.; Poumirol, J. M.; Rhodes, D.; Smirnov, D.; Pradhan, N. R.; Lin, Z.; Nguyen, M. A. T.; Elías, A. L.; et al. New First Order Raman-Active Modes in Few Layered Transition Metal Dichalcogenides. *Sci. Rep.* **2014**, *4*, 4215.
28. Wang, H.; Kong, D.; Johanes, P.; Cha, J. J.; Zheng, G.; Yan, K.; Liu, N.; Cui, Y.  $\text{MoSe}_2$  and  $\text{WSe}_2$  Nanofilms with Vertically Aligned Molecular Layers on Curved and Rough Surfaces. *Nano Lett.* **2013**, *13*, 3426–3433.
29. Tongay, S.; Zhou, J.; Ataca, C.; Lo, K.; Matthews, T. S.; Li, J.; Grossman, J. C.; Wu, J. Thermally Driven Crossover from Indirect toward Direct Bandgap in 2D Semiconductors:  $\text{MoSe}_2$  versus  $\text{MoS}_2$ . *Nano Lett.* **2012**, *12*, 5576–5580.
30. Chakraborty, B.; Bera, A.; Muthu, D. V. S.; Bhowmick, S.; Waghmare, U. V.; Sood, A. K. Symmetry-Dependent Phonon Renormalization in Monolayer  $\text{MoS}_2$  Transistor. *Phys. Rev. B* **2012**, *85*, 161403.
31. Ramakrishna Matte, H. S. S.; Gomathi, A.; Manna, A. K.; Late, D. J.; Datta, R.; Pati, S. K.; Rao, C. N. R.  $\text{MoS}_2$  and  $\text{WS}_2$  Analogues of Graphene. *Angew. Chem., Int. Ed.* **2010**, *49*, 4059–4062.
32. Jeffery, A. A.; Nethravathi, C.; Rajamathi, M. Two-Dimensional Nanosheets and Layered Hybrids of  $\text{MoS}_2$  and  $\text{WS}_2$  through Exfoliation of Ammoniated  $\text{MS}_2$  ( $\text{M} = \text{Mo}, \text{W}$ ). *J. Phys. Chem. C* **2014**, *118*, 1386–1396.
33. Berdemir, A.; Gutiérrez, H. R.; Botello-Méndez, A. R.; Perea-López, N.; Elías, A. L.; Chia, C.-L.; Crespi, V. H.; López-Urías, F.; Chalier, J.-C.; Terrones, H.; et al. Identification of Individual and Few Layers of  $\text{WS}_2$  Using Raman Spectroscopy. *Sci. Rep.* **2013**, *3*, 1755.
34. Sahin, H.; Tongay, S.; Horzum, S.; Fan, W.; Zhou, J.; Li, J.; Wu, J.; Peeters, F. M. Anomalous Raman Spectrum and Thickness-Dependent Electronic Properties of  $\text{WSe}_2$ . *Phys. Rev. B* **2013**, *87*, 165409.
35. Kipling, J. J.; Wilson, R. B. Adsorption of Methylene Blue in The Determination of Surface Areas. *J. Appl. Chem.* **1960**, *10*, 109–113.
36. Schniepp, H. C.; Li, J.-L.; McAllister, M. J.; Sai, H.; Herrera-Alonso, M.; Adamson, D. H.; Prud'homme, R. K.; Car, R.; Saville, D. A.; Aksay, I. A. Functionalized Single Graphene Sheets Derived from Splitting Graphite Oxide. *J. Phys. Chem. B* **2006**, *110*, 8535–8539.
37. Liu, T.; Li, Y.; Du, Q.; Sun, J.; Jiao, Y.; Yang, G.; Wang, Z.; Xia, Y.; Zhang, W.; Wang, K.; et al. Adsorption of Methylene Blue from Aqueous Solution by Graphene. *Colloid. Surface. B* **2012**, *90*, 197–203.
38. Yu, Y.; Huang, S.-Y.; Li, Y.; Steinmann, S. N.; Yang, W.; Cao, L. Layer-Dependent Electrocatalysis of  $\text{MoS}_2$  for Hydrogen Evolution. *Nano Lett.* **2014**, *14*, 553–558.
39. Tang, H.; Dou, K.; Kaun, C.-C.; Kuang, Q.; Yang, S.  $\text{MoSe}_2$  Nanosheets and Their Graphene Hybrids: Synthesis, Characterization and Hydrogen Evolution Reaction Studies. *J. Mater. Chem. A* **2014**, *2*, 360–364.
40. Bonanni, A.; Ambrosi, A.; Pumera, M. On Oxygen-Containing Groups in Chemically Modified Graphenes. *Chem.—Eur. J.* **2012**, *18*, 4541–4548.
41. Voiry, D.; Yamaguchi, H.; Li, J.; Silva, R.; Alves, D. C. B.; Fujita, T.; Chen, M.; Asefa, T.; Shenoy, V. B.; Eda, G.; et al. Enhanced Catalytic Activity in Strained Chemically Exfoliated  $\text{WS}_2$  Nanosheets for Hydrogen Evolution. *Nat. Mater.* **2013**, *12*, 850–855.
42. Frondel, J. W.; Wickman, F. E. Molybdenite Polytypes in Theory and Occurrence: II. Some Naturally-Occurring Polytypes of Molybdenite. *Am. Mineral.* **1970**, *55*, 1857.
43. Jaegermaa, W.; Schmeisser, D. Reactivity of Layer Type Transition Metal Chalcogenides towards Oxidation. *Surf. Sci.* **1986**, *165*, 143–160.
44. Miremadi, B. K.; Morrison, S. R. The Intercalation and Exfoliation of Tungsten Disulfide. *J. Appl. Phys.* **1988**, *63*, 4970–4974.
45. Lin, Y.-C.; Dumcenco, D. O.; Huang, Y.-S.; Suenaga, K. Atomic Mechanism of the Semiconducting-to-Metallic Phase Transition in Single-Layered  $\text{MoS}_2$ . *Nat. Nanotechnol.* **2014**, *9*, 391–396.
46. Lang, O.; Tomm, Y.; Schlaf, R.; Pettenkofer, C.; Jaegermann, W. Single Crystalline  $\text{GaSe}/\text{WSe}_2$  Heterointerfaces Grown by Van der Waals Epitaxy. II. Junction Characterization. *J. Appl. Phys.* **1994**, *75*, 7814–7820.
47. Eng, A. Y. S.; Ambrosi, A.; Chua, C. K.; Šanek, F.; Sofer, Z.; Pumera, M. Unusual Inherent Electrochemistry of Graphene Oxides Prepared Using Permanganate Oxidants. *Chem.—Eur. J.* **2013**, *19*, 12673–12683.
48. Bonde, J.; Moses, P. G.; Jaramillo, T. F.; Nørskov, J. K.; Chorkendorff, I. Hydrogen Evolution on Nano-Particulate Transition Metal Sulfides. *Faraday Discuss.* **2008**, *140*, 219–231.
49. Ambrosi, A.; Sofer, Z.; Pumera, M. Lithium Intercalation Compound Dramatically Influences the Electrochemical Properties of Exfoliated  $\text{MoS}_2$ . *Small* **2014**, *10*.1002/smll.201400401.
50. Kautek, W.; Gerischer, H. Anisotropic Photocorrosion of n-Type  $\text{MoS}_2$ ,  $\text{MoSe}_2$ , and  $\text{WSe}_2$  Single Crystal Surfaces: The Role of Cleavage Steps, Line and Screw Dislocations. *Surf. Sci.* **1982**, *119*, 46–60.
51. Murphy, D. W.; Di Salvo, F. J.; Hull, G. W., Jr.; Waszcak, J. V. Convenient Preparation and Physical Properties of Lithium Intercalation Compounds of Group 4B and 5B Layered Transition Metal Dichalcogenides. *Inorg. Chem.* **1976**, *15*, 17–21.
52. Tong, Y.; Lunsford, J. H. Mechanistic and Kinetic Studies of the Reactions of Gas-Phase Methyl Radicals with Metal Oxides. *J. Am. Chem. Soc.* **1991**, *113*, 4741–4746.
53. Bouroushian, M. *Electrochemistry of Metal Chalcogenides*; Springer-Verlag: Berlin, 2010.
54. Saji, V. S.; Lee, C.-W. Selenium Electrochemistry. *RSC Adv.* **2013**, *3*, 10058–10077.
55. Nicholson, R. S. Theory and Application of Cyclic Voltammetry for Measurement of Electrode Reaction Kinetics. *Anal. Chem.* **1965**, *37*, 1351.
56. Matsuda, H.; Ayabe, Y. Zur Theorie der Randles-Sevcík'schen Kathodenstrahl-Polarographie. *Z. Elektrochem.* **1955**, *59*, 494.
57. Song, C.; Zhang, J. Electrocatalytic Oxygen Reduction Reaction. In *PEM Fuel Cell Electrocatalysts and Catalyst Layers*; Zhang, J., Ed.; Springer: London, 2008; pp 89–134.
58. Wang, T.; Gao, D.; Zhuo, J.; Zhu, Z.; Papakonstantinou, P.; Li, Y.; Li, M. Size-Dependent Enhancement of Electrocatalytic Oxygen-Reduction and Hydrogen-Evolution Performance of  $\text{MoS}_2$  Particles. *Chem.—Eur. J.* **2013**, *19*, 11939–11948.

59. Karunadasa, H. L.; Montalvo, E.; Sun, Y. J.; Majda, M.; Long, J.; Chang, C. J. A Molecular MoS<sub>2</sub> Edge Site Mimic for Catalytic Hydrogen Generation. *Science* **2012**, *335*, 698–702.
60. Liao, T.; Sun, Z.; Sun, C.; Dou, S. X.; Searles, D. J. Electronic Coupling and Catalytic Effect on H<sub>2</sub> Evolution of MoS<sub>2</sub>/Graphene Nanocatalyst. *Sci. Rep.* **2014**, *4*, 6256.
61. Tsai, C.; Chan, K.; Abild-Pedersen, F.; Nørskov, J. K. Active Edge Sites in MoSe<sub>2</sub> and WSe<sub>2</sub> Catalysts for the Hydrogen Evolution Reaction: A Density Functional Study. *Phys. Chem. Chem. Phys.* **2014**, *16*, 13156–13164.
62. Xu, C.; Peng, S.; Tan, C.; Ang, H.; Tan, H.; Zhang, H.; Yan, Q. Ultrathin S-Doped MoSe<sub>2</sub> Nanosheets for Efficient Hydrogen Evolution. *J. Mater. Chem. A* **2014**, *2*, 5597–5601.
63. Konopka, S. J.; McDuffie, B. Diffusion Coefficients of Ferri- and Ferrocyanide Ions in Aqueous Media, Using Twin-Electrode Thin-Layer Electrochemistry. *Anal. Chem.* **1970**, *42*, 1741.